Jean-Hugues Beaux[1]
Safran Aircraft Engines,
Rond-point René Ravaud,
Moissy-Cramayel 77550, France
e-mail: jean-hugues.beaux@safrangroup.com

Julian Girardeau
Safran Aircraft Engines,
Rond-point René Ravaud,
Moissy-Cramayel 77550, France
e-mail: julian.girardeau@safrangroup.com

Sofiane Khelladi
LIFSE,
Arts et Métiers Institute of Technology,
CNAM,
HESAM University,
151 boulevard de l'Hôpital,
Paris 75013, France
e-mail: sofiane.khelladi@ensam.eu

Michael Deligant
LIFSE,
Arts et Métiers Institute of Technology,
CNAM,
HESAM University,
151 boulevard de l'Hôpital,
Paris 75013, France
e-mail: michael.deligant@ensam.eu

Christelle Perilhon
LIFSE,
Arts et Métiers Institute of Technology,
CNAM,
HESAM University,
151 boulevard de l'Hôpital,
Paris 75013, France
e-mail: christelle.perilhon@lecnam.net

Numerical Investigations of Flows and Heat Transfer in Turbine Disk Cavities

In gas turbines, the stator wells play a key role in the efficiency of the turbomachine. The research for performance gains requires a good understanding and an accurate modeling of the flows and heat transfers occurring in these areas. Within the framework of the European program main annulus gas path interaction (MAGPI) WP1, a two-stage axial turbine test rig provided an experimental database used to validate the computational fluid dynamics (CFD) models. The aim of this study is to setup a numerical methodology using the CFD solver ANSYS FLUENT *to accurately predict the conjugate heat transfer in the stator well area. The validation of the methodology relies on thorough comparison of the results with the MAGPI WP1 experimental temperature/pressure measurements. A geometry with axial cooling injection through lock plate slot was chosen. A Reynolds-averaged Navier–Stokes (RANS) three-dimensional sectorized CFD model of the turbine with conjugate heat transfer was used. It includes main gas path, cavities with labyrinths, disks rotor, the casing, and the nozzle guide vanes (NGV). Mixing planes are placed between the static and rotating frames. Different influences (mesh, turbulence model, thermal boundary conditions, radial labyrinths clearances) were studied and compared with experimental data. As a baseline, the first calculations were performed with a cooling flowrate chosen so that hot gas ingresses from the main stream into the stator well cavity. Good agreements between predicted and measured temperatures/pressures were observed, especially in the vicinity of the stator well. Discrepancies were spotted at the first rotor hub endwall and at the upstream wheelspace and will be discussed. Two other cooling configurations were conducted, one with cooling air exiting from the disk rim cavity to the main gas path and the other with the lowest cooling flowrate and so the highest ingress. Finally, the turbine performance under nonadiabatic conditions has been evaluated with an appropriate efficiency definition.*
[DOI: 10.1115/1.4065632]

Keywords: heat transfer, aerothermal modeling, turbine stator well

1 Introduction

The environmental constraints lead engine manufacturers to develop new technologies in order to reduce engines specific fuel consumption. This can be achieved by an improvement of the thermopropulsive efficiency, which can be done by an increase of either gas temperature or bypass ratio. Larger fan diameters can be used to increase the bypass ratio leading to an improved propulsive efficiency by reduction of the fan rotational speed. This contrasts with the turbine, for which the improvement of its efficiency leads to an increase of the rotational speed and a reduction of the stage count with a higher expansion ratio by stage. A gearbox can be used into the next engine generation in order to counteract this and decouple the fan and the turbine. Therefore, the design of high-speed low-pressure turbines brings new issues, especially for the turbine stator well (TSW) area.

Indeed, the amount of leakage air flowing through the turbine disk cavities is amplified due to the higher expansion ratio by stage. Moreover, as the rotational speed increases, the centrifugal loading on disks get worse. As the main gas path temperature exceeds the thermomechanical limit of the components, internal cooling systems are necessary. The cooling air is bled from the compressor and contribute poorly to the overall engine cycle. Furthermore, a spoiling effect appears where the cooling air re-enters into the main gas path, resulting on performance penalties. Therefore, it is

[1]Corresponding author.

desirable to reduce the amount of cooling air while maintaining the components integrity.

The cooling can be introduced axially or radially in the upstream disk cavity, where a complex flow field develops with a core flow and a disk entrainment flow driven by the rotor. Between the upstream and downstream parts, an interstage labyrinth seal is used in order to reduce the leakage of air. The seal flow depends mainly on the radial clearance and the pressure drop across the seal, which is a function of the upstream and downstream conditions including the pressure drop over the stage in the main annulus. Equation (1) is the St. Venant–Wentzell equation that enables the seal flow calculation

$$\dot{m} = C_D \cdot \frac{P_1 A}{\sqrt{T_{01}}} \cdot \left(\frac{P_2}{P_1}\right)^{\frac{1}{\gamma}} \sqrt{\frac{2\gamma}{R(\gamma-1)}\left[1-\left(\frac{P_2}{P_1}\right)^{\frac{\gamma-1}{\gamma}}\right]} \quad (1)$$

where index 1 and 2 stand for inlet and outlet, respectively.

The discharge coefficient C_D accounts for parameter like the seal clearance or the number of fins and can be determined experimentally or numerically. If the cooling flow is lower than the seal flow, ingress occurs into the cavity, with a mixing between the hot gas coming from the annulus and the cooling air. As the coolant flowrate increases and becomes greater than the seal demands, the remaining amount of cooling is ejected into the mainstream (egress).

In the framework of the main annulus gas path interactions (MAGPI) program, a two-stage turbine test rig has been developed with the aim of providing an experimental database to further advance in the understanding of cooling flow and annulus gas interactions and resultant heat transfer in the cavities. The data were also used to validate numerical methodologies. Dixon et al. [1] and Pohl [2] used a coupled finite element analysis (FEA)/Reynolds-averaged Navier–Stokes (RANS)-computational fluid dynamics (CFD) method to evaluate heat transfer in the turbine stator well with a good matching to the experimental data, especially near the stator. In the rotor hub endwall, the metal temperatures were underpredicted and only a coupled FEA to unsteady CFD, with the hot running geometry [2] managed to reduce the discrepancies. Smith et al. [3] and Da Soghe [4] used steady and unsteady conjugate methods that also achieved a good agreement with the experimental temperature measurements. A turbulence models sensitive study was performed by the authors [2–4], concluding that the ω-based models show the best agreement against experimental data. For the same test case, Lück et al. [5] used a thermal fluid structure interaction calculation to take into account the thermo-mechanical effects. A good matching was observed but the discrepancies at the rotor hub endwall could not be reduced. All of those validation studies were conducted with a radial inflow of cooling through holes drilled into the drive arm.

Guijarro Valencia et al. [6] did cooling optimization studies by evaluating different cooling concepts with adiabatic calculations. Regarding the cooling effectiveness of the disk rotor, they concluded that it is beneficial if the cooling is driven into the rotor disk boundary layer, in order to flood the cavity before leaking through the labyrinth seal. This can be achieved either by axial lock plate inlets in the rotor 1 or with a deflector plate when the cooling is insert radially through drive arm holes. This conclusion has been confirmed by Da Soghe [4] who evaluated the inclinations and positions of the drive arm holes.

In Sec. 2, a short overview of the rig is given. A configuration with an axial cooling injection through lock plate slots in the rotor 1 disk was chosen as case study. Indeed, this geometry seems promising in terms of cooling effectiveness [6,7] and, to the author's knowledge, conjugate heat transfer was never validated against this specific experimental data.

Then, the numerical methodology is presented in detail. The conjugate heat transfer study was conducted by setting up a three-dimensional (3D) sectorized RANS numerical model with the CFD code ANSYS Fluent. The domain represents the MAGPI turbine test rig with main gas path, cavities with labyrinths, disks rotor and blades, and casing and nozzle guide vanes (NGV). The hot geometry was used and an unstructured polyhedral mesh was generated.

In Sec. 4.4, results are presented for three cooling flow rates, allowing three configurations: high ingestion, low ingestion, and no ingestion (purge) of hot gas upstream of the second stator vane. A focusing has been done to the geometry and thermal boundary conditions of the upstream solid stator. Their impact on the TSW temperature prediction is shown. In contrast to prior investigations within the MAGPI project [1–5], the comparisons between calculation and temperature/pressure measurements have been extended to all the available measures, including the TSW area as well as the upstream cavity, main gas path and the casing. The mesh and turbulence model influences are assessed. Furthermore, the uncertainty coming with the prediction of hot running geometry is presented. Hence, the impact of the radial labyrinths clearances on the accuracy of the calculations are discussed.

2 Turbine Test Rig Description

The experimental setup of the test rig is described in detail by Coren et al. [7] and Eastwood [8]. The test section of the rig comprises a two-stage axial turbine, rated at 400 kW with a pressure ratio of approximately 2.7 at the design point speed of 10,630 rpm. The main annulus air is supplied to the rig by an adapted aero engine driven compressor plant at 4.8 kg s^{-1}, at a pressure of 3.3 bar, and a total temperature of 443 K. An Atlas Copco screw type compressor is used to provide the various cooling supplies. The rig test section (Fig. 1) has been design to represent the key features of a TSW. Each turbine stage has 39 NGV and 78 blades to suit a simulation using a periodic sector model. The rotational Reynolds number in the cavity is approximately 1.8×10^6 at the design point.

The internal cooling system is represented in Fig. 1. The cooling air (named as coolant) is supplied to the upstream stator well either radially through drive arm holes with removable threaded inserts or axially through lock plate slots with removable cover plates. This arrangement allows 0, 13, 26, or 39 flow exits to be used at each entry point, which enables different cooling jet velocities for a given coolant flowrate. Variations of cooling are performed to create either ingress or egress conditions at the rim seals. In order to ensure an accurate amount of cooling air into the TSW, every cavity adjacent to the coolant flow path was balanced to the pressure of the coolant flow. This is achieved by balance flow pressure tuning in the upstream wheelspace and guarantees that there is no mass flow added or subtracted to the coolant flow path. The excess air from the pressure balance process is vented out of the wheelspace to prevent egress into the main annulus. However, during the first test phase, they were defaults on the pressure taps in the wheelspace leading to

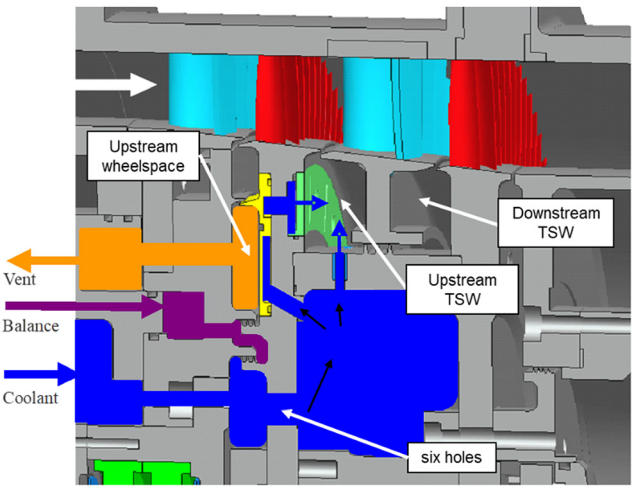

Fig. 1 A cross section of the test rig, with internal cooling system

nonbalanced cavity seals and thus an increase of the coolant flow rates injected into the TSW. More details are given by Eastwood [8].

The TSW and surroundings areas are heavily instrumented with metal and air thermocouples as well as static pressure tapings. Turbine main annulus conditions are measured by temperature and pressure probes built into the leading edges of the NGV and with metal thermocouples on the casing. All the instrumentations are depicted in Fig. 2.

3 Numerical Methodology

The CFD modeling is detailed in this part, with a special attention being paid to the geometry. The study has been performed with the CFD solver ANSYS FLUENT.

3.1 Computational Fluid Dynamics Domain. The 3D CFD domain, displayed in Figs. 3 (fluid domain) and 4 (solid domain) is a 1/39th sector part of the full test rig containing one stator vane and two rotor blades for each of both stages. The rotor solid domain includes the R1 and R2 blades, disks with screws in the coolant passage and the drive arm with the labyrinth fins. The stator solid domain contains the S1 and S2 blades, the stator foot, the casing, and the upstream and downstream components. The rotor is made of Titanium alloy (TiAl6V4) and the stator of Stainless Steel 304 (SS304). In order to take into account the thermal diffusion into the first stator disk, the balance and vent air holes (detailed in Fig. 1) are adapted to the sector by adjusting their size to respect a volume equivalent to the real holes. Thermal resistances are added between the two solids into the first stator disk to simulate radial and axial clearances, as displayed in Fig. 4. The impact of these resistances is detailed in the results part. The fluid domain is illustrated in Fig. 3 and includes all the cavities, main gas path, the stator well, and the cooling system with the axial slot. The calculation is set with multiple reference frames. The moving and static parts of the fluid zones are displayed in Fig. 3. General Turbo-Interface mixing planes are used in the main annulus gas path with the same pitch. They are placed in such a way that the stator well and blades passage of both stages are joined in the same moving domain. The asymmetrical holes of the first stator disk enforce the use of a static fluid part in the upstream wheelspace. This area is connected to the moving part by axisymmetric interfaces without interpolation. In contrast with the prior investigations, the second mixing plane is titled to prevent it from being too close to the stator 2 leading edge. The boundary conditions are defined according to the measurement conditions given by Eastwood [8]. The main annulus is set with uniform total pressure and temperature at the inlet and with a radial equilibrium static pressure at the outlet. The inlet and outlet of the main gas path are placed as far as possible from the stator well. The in- and outlets in the wheelspace use a fixed mass flowrate and total temperature.

Empirical heat transfer coefficients are used to apply forced convection boundary conditions on the wall of the upstream first stator disk and the casing. All fluid–solid interfaces flux are set by conjugate heat transfer. Any remaining wall is set to be adiabatic. Walls motion is set where applicable.

In the test rig, the six holes in the rotor 1 (indicated in Fig. 1) are incompatible with the 1/39th sector model. As was done by Smith et al. [3], these holes are replaced by 39 slots that have a cross section defined (by a separate CFD study) to match the mass flowrate of the six holes for the same pressure ratio.

The hot running conditions are considered to set the radial labyrinths clearances:

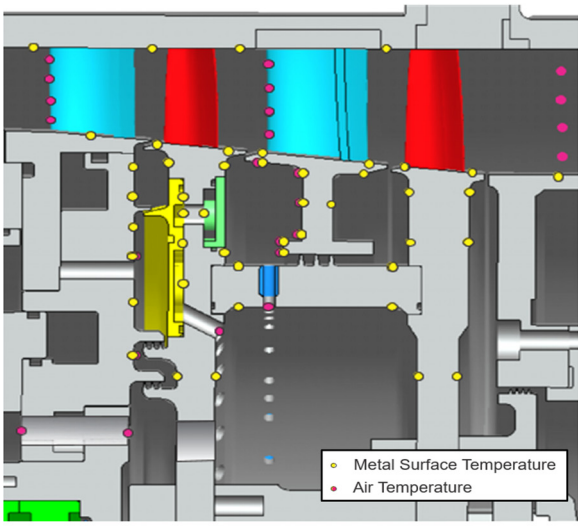

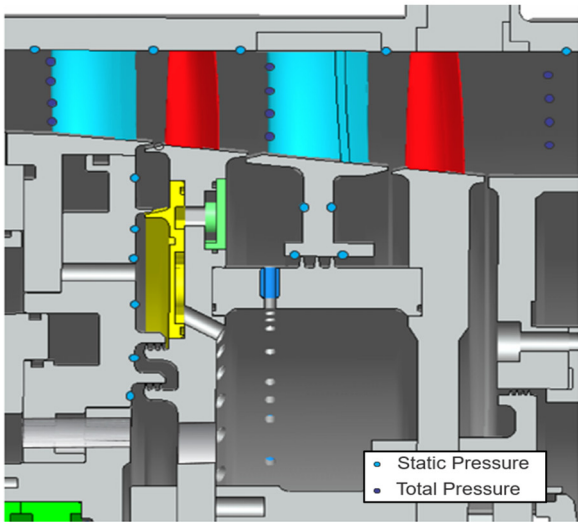

Fig. 2 Temperature and pressure instrumentation

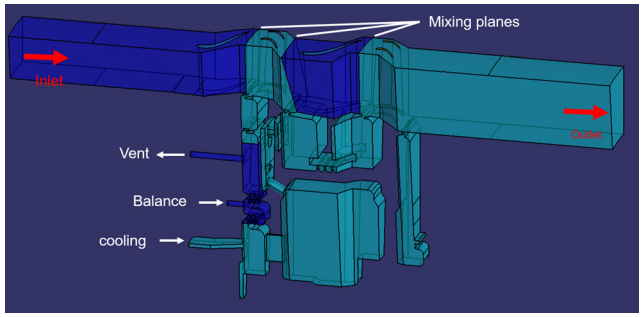

Fig. 3 Fluid domain

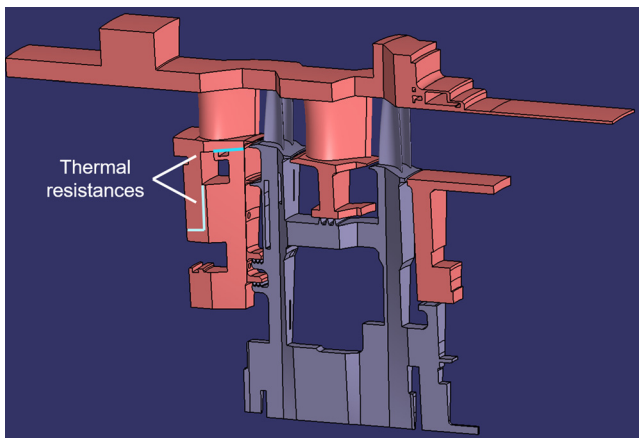

Fig. 4 Solid domain with thermal resistances

- For the labyrinth seal into the stator well area, hot clearances were measured for each cooling flow rates with a radial sensor and the data are given with their uncertainties by Eastwood [8]. Thus, these hot clearances are used to set the radial labyrinth clearance into the TSW area. A sensitive study was conducted to evaluate the impact of the sensor uncertainties on the accuracy results;
- For the labyrinths seals in the upstream wheelspace, no data were available, so a FEA model was set up to estimate hot clearances. However, discrepancies against radial displacements experimental measures in the stator well area were observed and significant uncertainties remains.

Thus, all these uncertainties coming from the estimation of hot running clearances are benchmarked against experimental data in the results section.

Then, the tip clearances are not modeled. However, the rotor–stator conductive heat flux is disabled between the blade tips and the casing.

Finally, accuracy of the results was tested for three cooling flow rates. All the cooling flows are expressed as a percentage of the main annulus flow (%MF):

- The first one with a low coolant flow (0.8%MF) named as reference case, with ingestion of hot gas through the R1/S2 rim seal;
- The second one named as purged cavity case, with a higher coolant flow (1.2%MF) that allows the cavity to be fully purged;

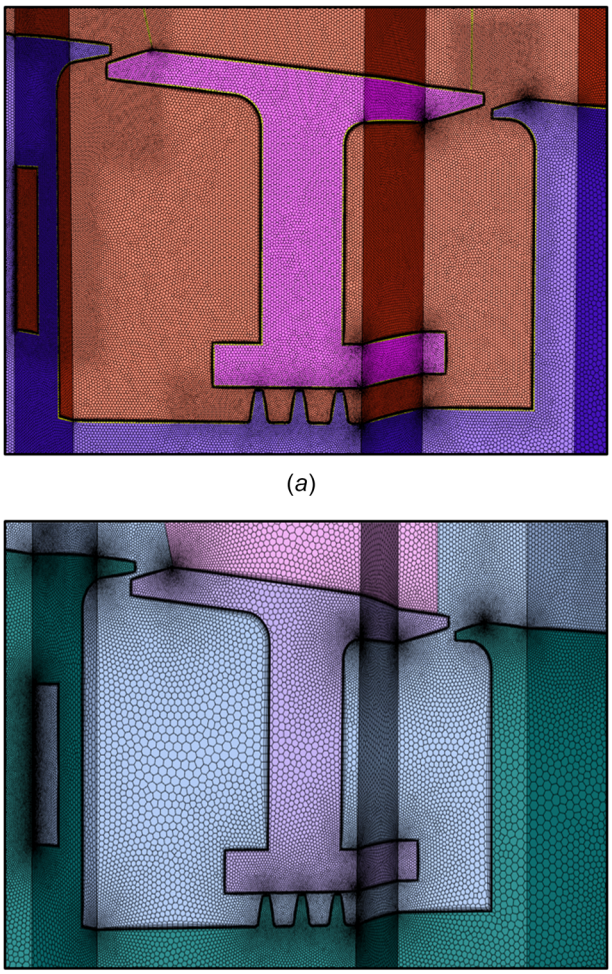

(*a*)

(*b*)

Fig. 5 Comparison of stator-well meshes: (*a*) fine and (*b*) intermediate

- The last one named as strong ingress case with the lowest cooling flow rate (0.6%MF) used during the MAGPI test campaign.

3.2 Mesh Generation. The mesh was generated with ANSYS FLUENT Meshing and is an unstructured polyhedral mesh for the fluid and the solid. Two cases were created (named as "fine" and "intermediate" meshes) to study the influence of the mesh on the solution. The fine mesh counts 36 million cells including 26 million fluid elements whereas the intermediate mesh has 23 million cells for 16 million fluid elements. The meshes of the TSW are displayed in Fig. 5. They include a refinement in the TSW area with a body of influence.

The mesh density is controlled by the cells max size parameter.

Both grids share the same cells min size and boundary layer. Thus, only inflation polyprisms aspect ratio is deteriorated between the two cases. The $y+$ criteria reaches a maximum of three in the whole domain and is less than one in the refined stator well area. Several criteria were satisfied for both meshes:

- Orthogonal quality greater than 0.15
- 12 layers of polyprisms in the boundary layer
- An aspect ratio of 400 and 800 for the fine and intermediate mesh, respectively.

No impact on the results was observed between the two meshes. Consequently, the 36 million mesh is fine enough and has been used for all the calculations.

3.3 Solver Setup. The RANS equations were solved using a second-order finite volume discretization with compressible flow and viscous work. Two turbulence models were tested (k–ω SST and k–ε realizable). The k–ω SST with near wall resolved boundary layer was selected as it offers lower computation times and combines the advantages of both ε and ω-based models. Moreover, it proposes better results in the vicinity of the stator foot, as shown in Sec. 4.2. The production limiter option was selected [9]. The air properties are temperature dependent and the ideal gas hypothesis is used. The thermal conductivity λ was set with the kinetic-theory and the dynamic viscosity μ with the Sutherland's law. The solids materials properties are also temperature dependent.

The convergence of the steady-state solution was assessed by monitoring the mass, momentum, energy, and turbulence model residuals. The mass and turbulence model residuals are less than 5×10^{-3} whereas momentum and energy residuals reach values below than 2×10^{-6}. Then, the main properties like the inlet mass flowrate, outlet total temperature, wall moments, as well as all points corresponding to rig measurements were monitored to help judging convergence. The main properties imbalances are less than 0.1%. The measurement points monitoring shows that more than 5000 iterations are necessary to reach convergence of the metal and air temperatures. Temperature variations remain (± 0.5 or 1 K depending on the areas) but are still acceptable.

4 Results and Discussion

The results are first presented for the reference case (0.8%MF) with a comparison against experimental data in the whole domain. The influence studies carried out in this case are displayed where relevant.

Then, as mentioned in Sec. 3, the influence of the cooling flow on the simulation accuracy is assessed with two cases (Sec. 4.4):

- Purged cavity case also named as 1.2%MF case
- Strong ingress case also named as 0.6%MF case

For each of these cases, comparisons between experimental and computational results are shown for different areas of the domain with special attention given to the TSW.

The ingress or egress configurations were confirmed for the three cases by a flowrate assessment over the entire domain.

As mentioned in the previous part, the fine mesh was used for all results presented here. Excepted for the turbulence model sensitivity, the k–ω SST was retained for all the calculations.

All the calculated values were extracted either with an azimuthal mass-weighted average for the air temperatures or with an azimuthal area-weighted average for the metal temperatures and static pressures, at the radial and axial locations of the sensors.

The error bars on the graphs represent the uncertainty of temperature measurements when applied on the experimental data and are equal to ± 0.3 K [8]. When applied on the numerical results, error bars indicate the numerical uncertainty (variation of the computed values over the last 500 iterations).

Since the MAGPI test rig is colder than actual engines, results' accuracy criterion must be defined with respect to actual engine operating conditions. Thus, a relative precision is defined, based on the actual engine operating conditions

$$\varepsilon = \frac{T_{m_{\text{CFD}}} - T_{m_{\text{engine}}}}{T_h - T_c} \tag{2}$$

where T_m is the metal temperature, and T_h and T_c stand for the hot and cold temperature defined as air temperature at leading edge of NGV 2 and air cooling temperature at the cavity inlet, respectively.

Then, an accuracy requirement was defined as follow:

$$\varepsilon < 0.07 \tag{3}$$

It is based on the Safran's needs with regard to this numerical methodology. A transposition of this requirement to the MAGPI test rig operating conditions leads to

$$\Delta T_{\text{calculation/measure}} = 3\,^{\circ}C \tag{4}$$

Therefore, this criterion will be used to assess the accuracy of this methodology with respect to requirement based on the actual engine operating conditions.

4.1 Main Annulus—Reference Case. First, the main gas path mass flow was compared with experimental data and it was found that it is 1.35% under-estimated by the simulation, which is close to the sensor uncertainty ($\pm 1.3\%$).

Comparisons between temperatures and pressures with experimental data at the leading edge of the vane 2 are shown in Fig. 6. The agreement with experimental data is quite good in that area.

At the main annulus outlet, total temperatures are slightly under-estimated by the CFD with values varying between 2.5 and 4.5 K from the middle to the top of the annulus.

Temperatures at the inner part of the casing were also benchmarked against experimental values. Important discrepancies were observed and attributed to the tip clearances being not modeled. In the rig, the leakage flow passing through those clearances are not expanded and warm up the casing in contrast with the simulation where the expanded gas have lower temperature leading to a strong underestimation (from 6 to 15 K) of the casing metal temperatures. In addition, analytical calculation shows that temperature at the inner diameter is very weakly driven by the empirical convective conditions applied on the casing outer diameter.

4.2 Upstream Wheelspace and Stator Well Area—Reference Case. Figure 7 presents static pressures into the turbine stator well. A good accuracy of the calculation is observed which means that the simulation well predicts the pressure drop across the labyrinth seal.

In the upstream wheelspace, the influence of the thermal resistances on the metal and air temperatures is assessed and displayed in Fig. 8. In this area, simulation gives higher metal temperatures than measured. A flux assessment made on the first stator disk has shown that the mainly hot source is the conductive flux coming from the main gas path. The convective flux between the upstream wheelspace fluid and solid stator is less significant. Following those findings, thermal resistances were added into the model. In particular, a better analysis of the rig assembly concludes that the centering just under the NGV hub is loose. The resistances reduce the conductive flux and thus give better results. There are still persisting discrepancies, which could be reduced by improving the thermal resistances geometry or the boundary conditions at the upstream face of the stator disk. However, the impact of the resistances is confined on the upstream wheelspace so the

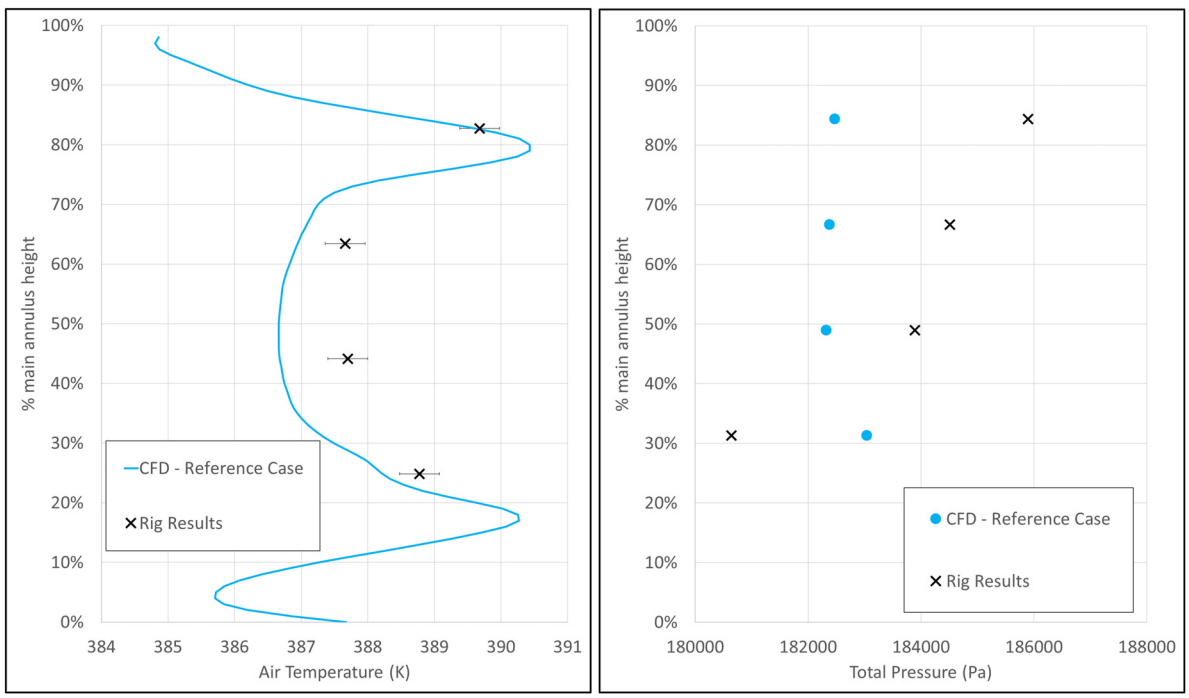

Fig. 6 Total temperature and pressure at NGV-2 leading edge rake

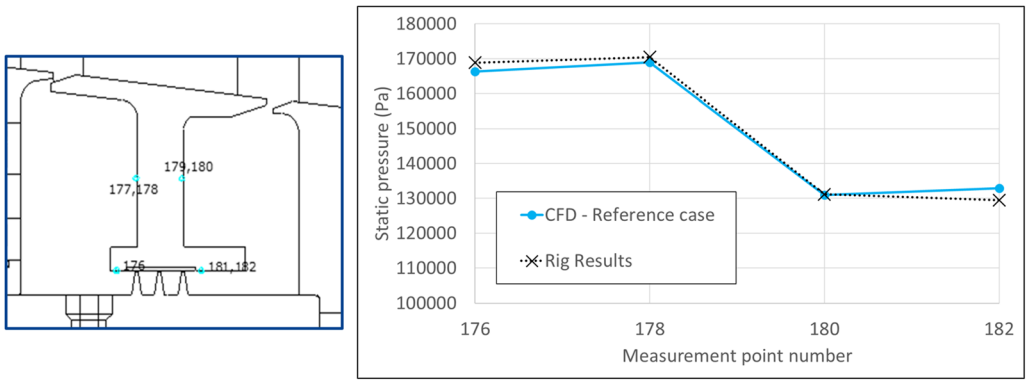

Fig. 7 Stator foot static pressure in the TSW area

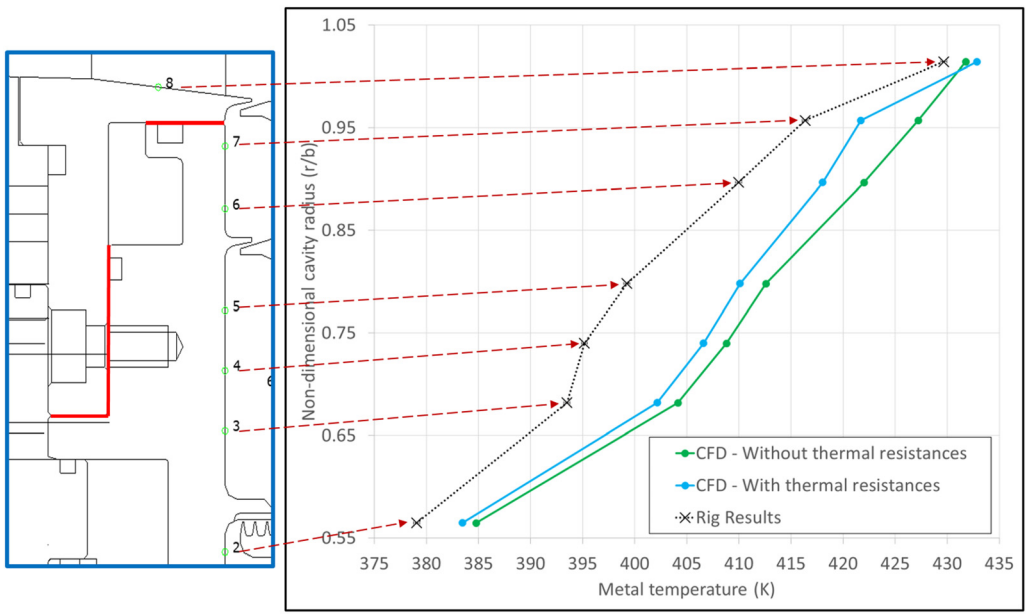

Fig. 8 Metal temperature at the downstream face of the first stator disk—thermal resistances influence

improvement of those features is out of the scope of this study which primarily focusing on the stator well area.

Figure 9 displays the comparison between metal temperatures with experimental data at the downstream of the rotor 1 disk. Comparison with air temperature at the inlet of the lock plate feed cavity is also added on Fig. 9 and is spotted by circle and triangle. Similar results are observed at the upstream face of this rotor 1 disk.

Alike to prior investigations [1–6], the simulation under-predicts the temperature measurements at the first rotor hub endwall, probably due to a limitation of the RANS model. As found by Pohl [2], only an URANS simulation is able to correctly predict this area, which is probably driven by unsteady and fully turbulent phenomena. However, the cooling air temperature into the lock plate feed cavity (measurement points (MP) number 103, 104, 105 outlined in Fig. 9) is accurately predicted by the simulation. Thus, the reasonable differences between predicted and measured temperatures found in the rotor 1 disk are a consequence of the under-predicted heat transfer in the rim gap region.

In the stator well area, Figs. 10 and 11 show a good agreement between predicted and measured air and metal temperatures. Therefore, in the zone of interest and far from the uncertainties coming with the boundary conditions, the simulation offers results with a very good accuracy. The main deviation is observed close to rim seal region where the experimental trend between MP25 and MP26 is not predicted by the simulation. As stated by Pohl [2] and Smith et al. [3], the steady-state approach does not allow local ingress/egress effects in the rim seal to be captured. This could explain the slight discrepancy observed in MP25.

The radial clearance of the TSW labyrinth was modified in the range of the measure uncertainty given by Eastwood [8]. Three radial clearances were tested (0.401 mm–0.425 mm–0.449 mm). The ingress mass flowrate increases with the increasing radial clearance. However, as resumed in Table 1, this mass flow is weak compared to the cooling flow. Thus, the metal and air temperatures are not significantly impacted by this influence (less than 1.5 K difference between configurations).

Turbine stator well temperatures might be further affected in a case where the ratio between coolant and ingress mass flow would be lower.

As mentioned previously, two turbulence models were tested (k–ω SST and k–ε realizable). A small influence of the model was observed in the vicinity of the stator foot and showed that the k–ω SST gives the more accurate results, with respect to the experimental measures. Figures 12 and 13 show the influence of the turbulence model on the metal and air temperatures on the stator foot.

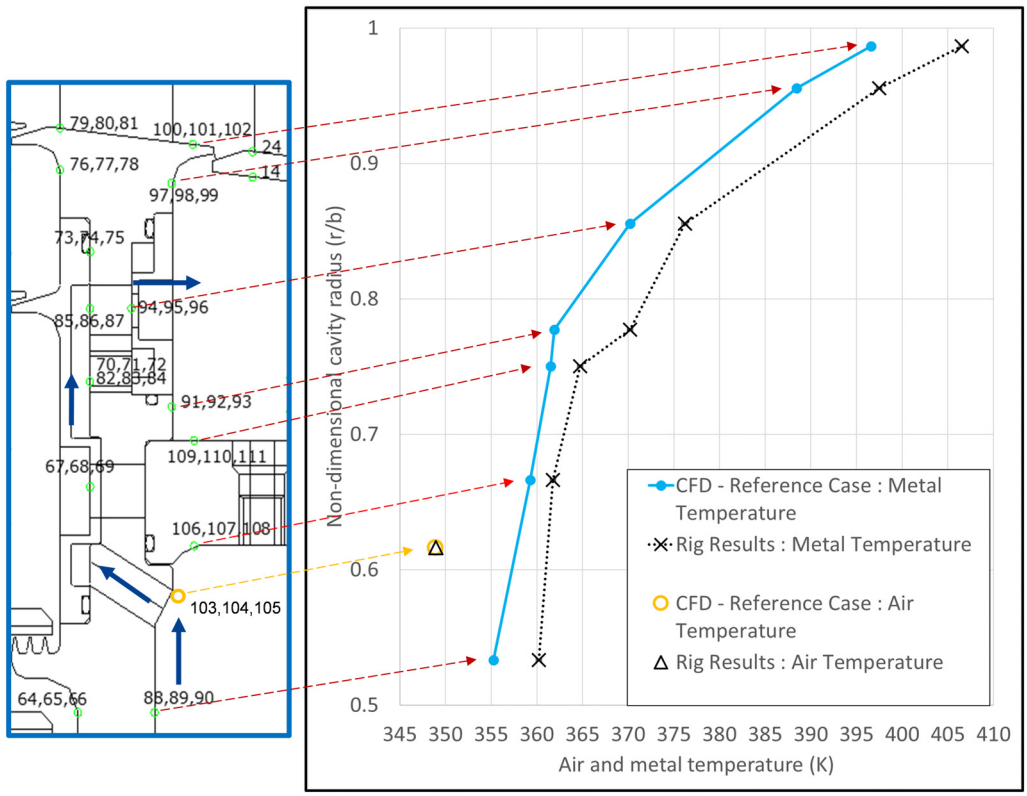

Fig. 9 Metal temperature at the downstream face of the first rotor disk and air temperature at the inlet of the lock plate feed cavity

A mass flowrate assessment shows less ingress for the k–ε model, which is a consequence of a smaller labyrinth seal mass flow (1.2%MF for the k–ε against 1.23%MF for the k–ω SST). Several reasons could explain this mass flow reduction:

- Modification of the main annulus flow by the turbulence model, which changes the cavity pressure ratio
- Modification of the total temperature at the inlet of the labyrinth seal
- Modification of the discharge coefficient Cd by modification of the flow inside the labyrinth

The contribution of each of these factors to the change in labyrinth mass flowrate can be quantified using the St. Venant–Wentzell Eq. (1), as resumed in the following table. The last column indicates the percentage of contribution of each cause to the change on the labyrinth mass flow, by comparison to the reference value given by the k– ω SST model.

Table 2 indicates that the impact of the k–ε turbulence model on the Cd represents 95.6% of the labyrinth mass flow drop and is then the major contributor.

Despite a lower ingress level for the k–ε, the air and metal temperatures given by this turbulence model are warmer than those given by the k–ω SST. This could be explained by higher convective heat transfer on the NGV 2 and on the stator foot for the k–ε model, as depicted in Fig. 14. Indeed, the k–ε model predicts a higher average skin friction coefficient, which leads to higher heat transfer coefficient. By conduction, the stator foot temperatures are then hotter for the k–ε model.

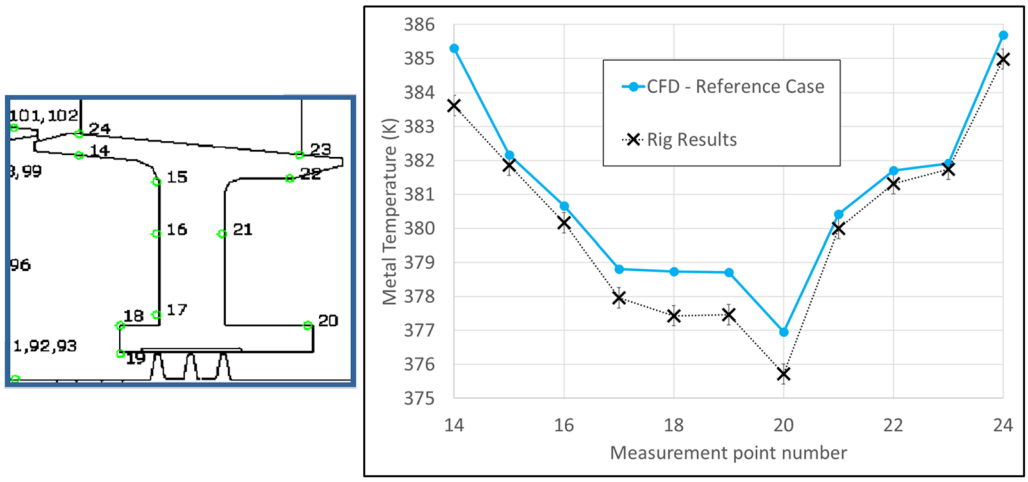

Fig. 10 Stator foot metal temperature in the stator well

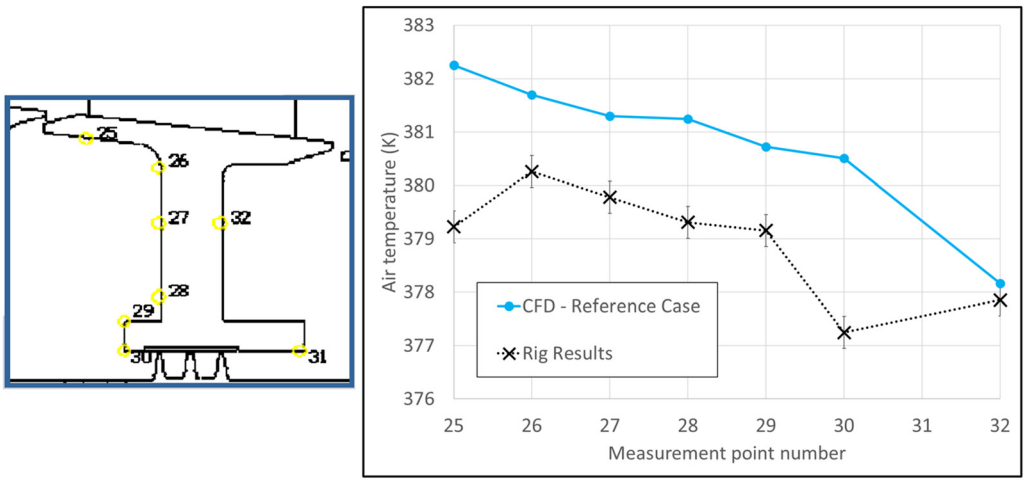

Fig. 11 Air temperature on the stator foot in the stator well

Table 1 Influence of the radial clearances on the mass flow into the TSW

Clearances (mm)	0.401	0.425	0.449
Cooling mass flow (g/s)	49.1	49.2	49.0
Ingress mass flow into the TSW (g/s)	5.6	9.2	14.6
Labyrinth seal mass flow (g/s)	54.7	58.4	63.6

For the air temperatures, there are two antagonistic effects:

- More ingress predicted by the k–ω SST model, which leads to hotter air temperatures with this model
- A hotter solid temperature of the stator with intensified convective heat transfer for the k–ε model, which leads to warmer air temperature with this model.

Since the air temperatures are hotter in the k–ε model, the second effect may be dominant over the first one and could explain these results.

In the other regions of the domain, the differences between turbulence models prediction are lower than the numerical variations and cannot be interpreted. Finally, and according to previous studies, the k–ω SST model gives better results and faster convergence and was then used for all the calculations.

On the upstream face of the rotor 2, the metal temperatures are slightly under-estimated by the calculation. This is probably due to an under-estimation of the local convective heat transfers on the rotor 2 endwall due to the limitation of the RANS model to capture unsteady phenomena (Fig. 15).

4.3 Influence of the Radial Clearance of the Upstream Wheelspace Labyrinths—Reference Case. As mentioned in the methodology part, the FEA model used to estimate the hot running clearances of the two upstream wheelspace labyrinths brings uncertainties. To overcome that, another calculation has been carried out with different radial clearances. For each calculation, the same radial clearance is applied for the two labyrinths:

- The baseline had the radial clearances given by the FEA model (0.2 mm) and named as hot clearances case;
- The influence has smaller clearances (0.15 mm). It fits with the cold geometry and named as cold clearances case.

The thermal resistances mentioned earlier were set for these two cases.

A flowrate assessment is presented in Fig. 16. The values are displayed in the upper and the lower boxes of the tables for the hot and the cold clearances case, respectively. The mass flows are

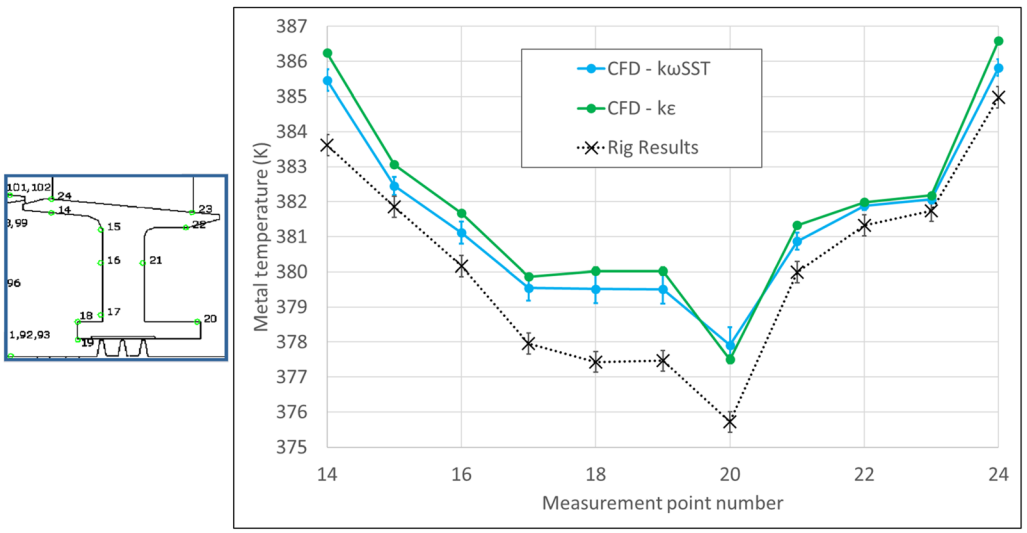

Fig. 12 Stator foot experimental and numerical metal temperatures—turbulence model influence

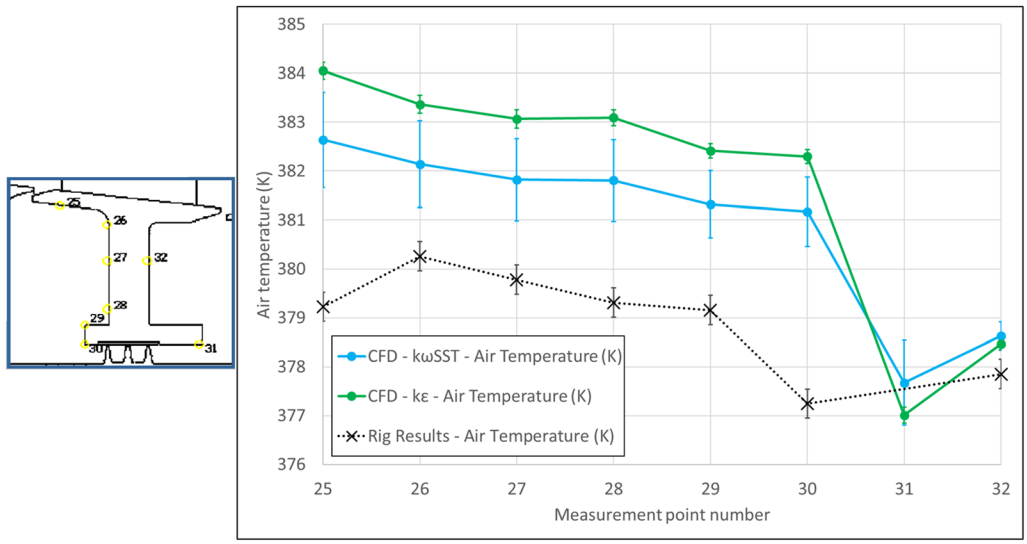

Fig. 13 Stator foot experimental and numerical air temperatures—turbulence model influence

Table 2 Contribution of the different phenomena on the labyrinth mass flow drop between the *k–ε* and *k–ω* SST predictions

Causes	*k–ε*	*k–ω* SST	Impact on the labyrinth mass flow rate
Cavity pressure ratio (P_2/P_1)	0.760	0.758	−10.9%
T_{01}	376.93	378.06	+6.5%
Cd labyrinth	0.593	0.606	−95.6%

expressed as a percentage of the main annulus flow. Moreover, the flow rates of the upstream labyrinths are indicated in Table 3. The smaller clearances lead to a reduction of the ingress mass flowrate through the S1/R1 rim seal.

Thus, as shown in Fig. 17, the metal temperatures at the downstream face of the stator 1 are reduced with the cold build.

This strong trend is also observed on the air temperature in the upstream wheelspace. In that area where the simulation over-predicts the temperatures, this influence is valuable for the accuracy of the calculation.

As the cold radial clearances reduce the hot gas ingress into the upstream wheelspace, the coolant temperatures at the inlet of the lock plate feed cavity are reduced for the cold clearances case (Table 4).

The metal temperatures in the up- and down-stream face of the first rotor disk are also reduced (between 1 and 3.5 K) by the diminution of the radial clearances. Two effects can explain that reduction:

- The drop of the coolant temperature reduces the heat flux between the lock plate feed cavity and the solid rotor
- The drop of the hot gas ingress through the S1/R1 rim seal reduces the heat flux between the upstream wheelspace and the solid rotor

With the hot clearances case, the coolant temperature is well predicted by the simulation (Fig. 9) whereas the cold clearances case under-estimates those temperatures. Thus, it seems that the clearances calculated by the FEA model are accurate.

Finally, it is observed that (as for the thermal resistances) the impact of this influence is limited to the upstream wheelspace and rotor 1 disk and does not changes the simulation accuracy in the TSW.

To conclude, even if the cold build gives better results in the upstream wheelspace, this influence leads to an under-estimation of

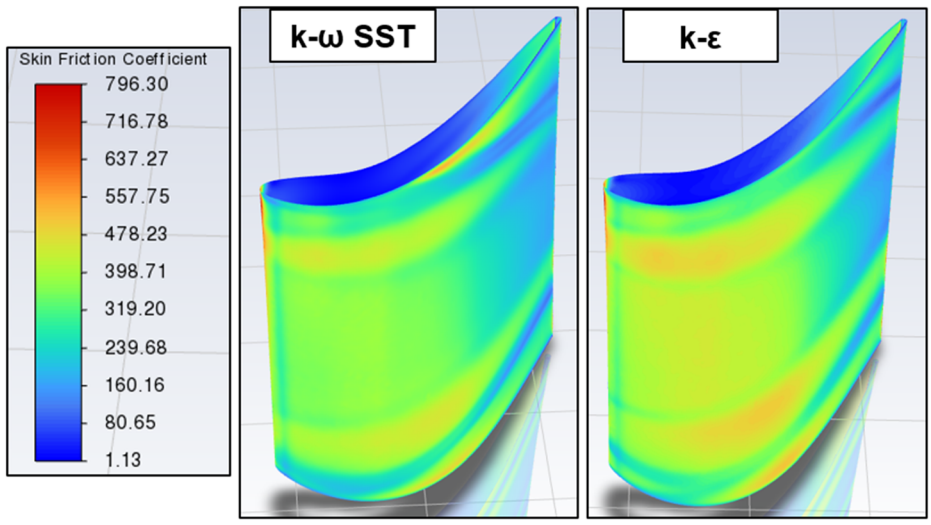

Fig. 14 Influence of the turbulence model on the skin friction coefficient on the NGV 2

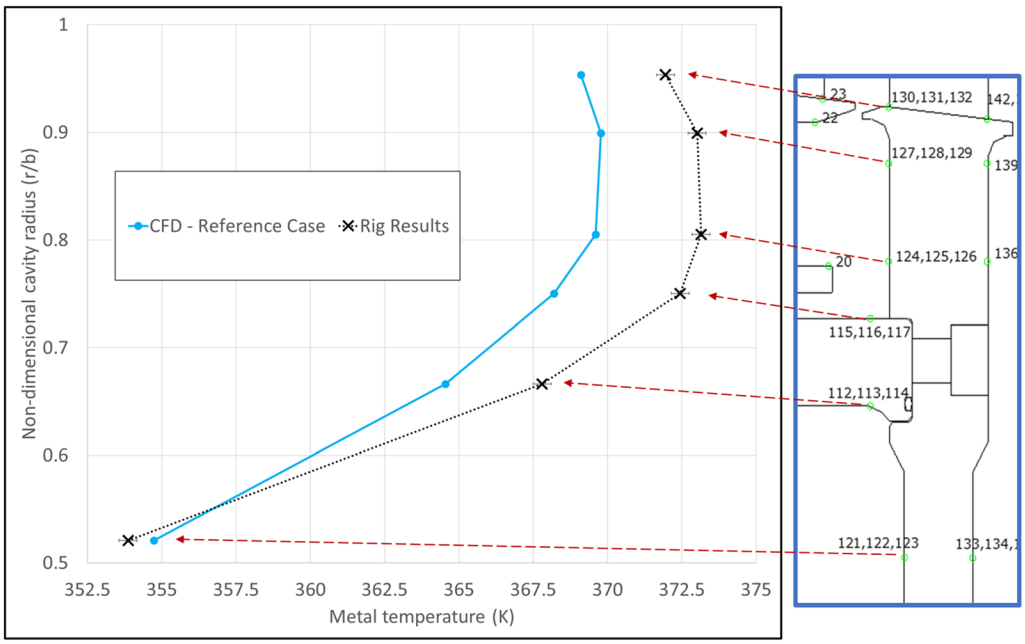

Fig. 15 Metal temperature at the upstream face of the second rotor disk

the coolant temperature at the inlet of the lock plate feed cavity. The metal temperature on the first stator must be improved by another manner like tuning the thermal boundary conditions on the upstream face.

This influence highlights the need for accurate ingress predictions when axial throughflow is weak and the importance of taking into account hot builds to accurately predict cooling mass flow distributions.

4.4 Influence of the Cooling Mass Flow Rate. After benchmarking the numerical methodology with a low cooling flowrate, the accuracy of the simulation is presented for two other cooling configurations:

- One with higher cooling flow leading to egress of gas through the R1/S2 rim seal, which means a purged cavity and named as 1.2% case
- The other with lower cooling flow leading to stronger ingress into the cavity and named as 0.6% case

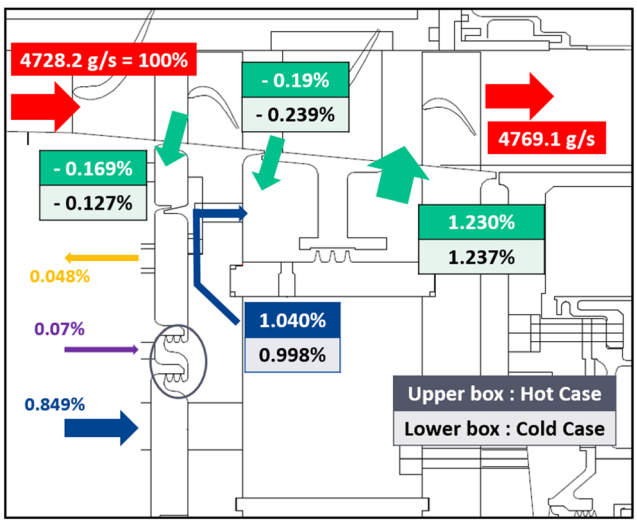

Fig. 16 Flow rate assessment over the whole domain with influence of the hot geometry in the upstream wheelspace

The fine mesh and k–ω SST turbulence model were used. Thermal resistances were placed into the first stator disk.

For the purged cavity case, radial clearance of the TSW labyrinth seal was given by Eastwood [8]. On the contrary, no radial clearances data were available for the 0.6% case so a linear interpolation was used, based on the two other cases, to set the radial clearance of the TSW labyrinth. The FEA model was not used to calculate the upstream labyrinths clearances as it gave results with strong inaccuracy. Thus, the same clearances (equal to the reference case) were set for the 0.6% and 1.2% cases. The consistency of the imposed clearances was verified by comparison with the experimental data.

Figure 18 shows a flowrate assessment over the whole domain for the three cases. The values for the 0.6% (strong ingress case), 0.8% (reference, with ingress), and 1.2% cases (purge case) are displayed in the top, middle, and bottom boxes of the tables. For all cases, the cooling flow rates imposed upstream of the domain (coolant, balance, and vent) bring the desired flow configuration into the turbine stator well cavity (strong ingress, ingress, and egress at the R1/S2 rim seal).

As for the reference case, the main gas path mass flow was compared with experimental data for the 0.6 and 1.2% cases and it was found that it is 1.47% and 1.28% under-estimated by the simulation, which is close to the sensor uncertainty (±1.3%).

The total temperatures at the leading edge of the stator vane 2 are well predicted by the simulation, with the same precision for the three cases.

The comparisons with the temperature and pressure measurements into the cavities are presented from the upstream to the downstream of the domain, following the cooling flow in the test rig.

Table 3 Upstream wheelspace labyrinth seals flow with influence of the hot clearances

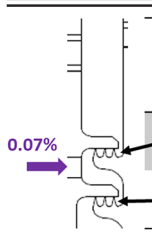

	Hot clearances (0.2mm)	Cold clearances (0.15mm)
Upper labyrinth seal flow	0.121%	0.078%
Lower labyrinth seal flow	0.191%	0.148%

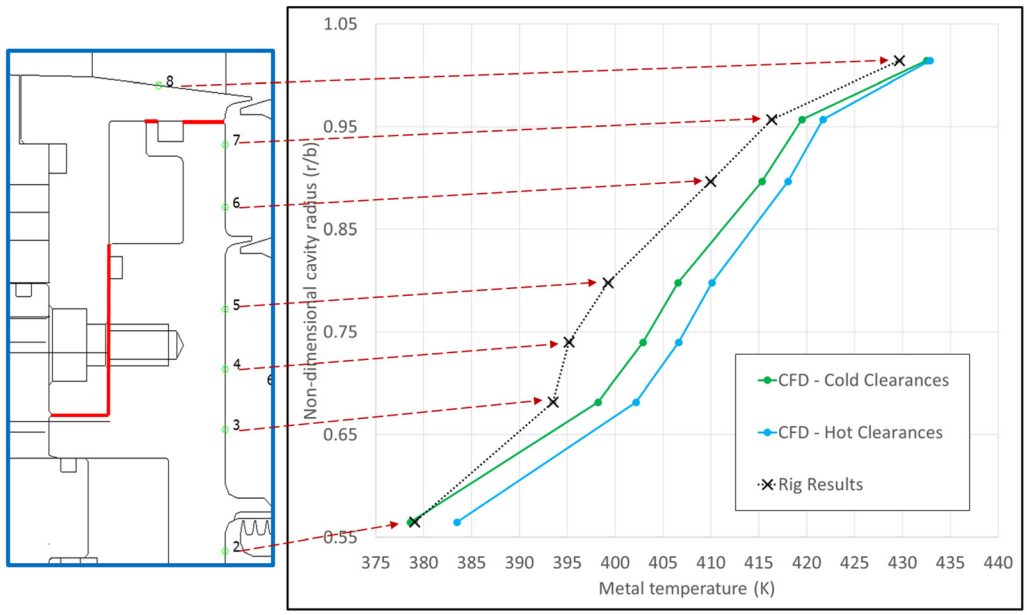

Fig. 17 Metal temperature at the downstream face of the first stator disk—radial clearances influence

Table 4 Air temperatures at the inlet of the lock plate feed cavity—radial clearances influence

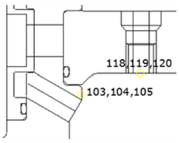

	Hot clearances	Cold clearances	Rig Results
MP 103-105 (K)	348.9	346.9	349.0
MP 118-120 (K)	358.1	356.3	358.8

In the upstream cavity, Fig. 18 shows a different behavior between the two ingress cases (0.6% and 0.8%) and the egress case (1.2%). The first two cases show an introduction from the main gas path into the upstream cavity, which is mixed with the cooling flow at low radius. On the contrary, this introduction is weaker for the 1.2%MF case and is ejected with the vent flow without mixing with

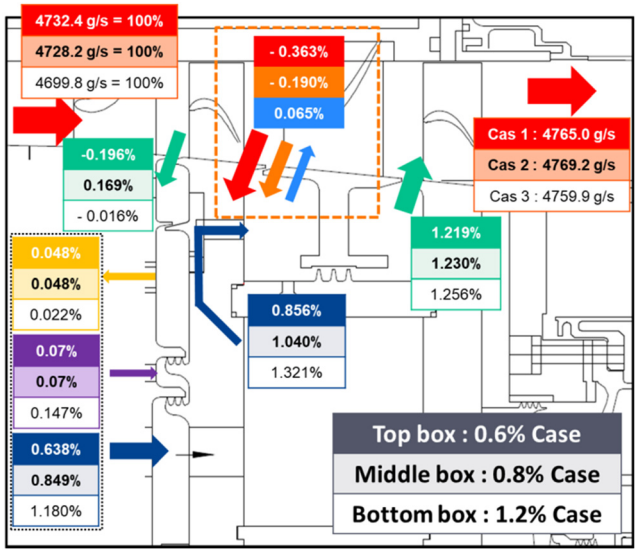

Fig. 18 Flow rate assessment over the whole domain for the three cooling configurations

the cooling flow. As shown in Fig. 19, this behavior modification affects the accuracy of the simulation. Although the simulation still overestimates the metal temperatures at the downstream face of the stator 1, the 1.2%MF case shows a better agreement with the experimental data (the discrepancies are reduced by 2–6 K depending on the radius). Indeed, as the ingress flow is ejected through the vent hole, the convective heat transfer at the lower part of the stator disk occurs only with the known temperatures imposed (in accordance with the experimental data) at the inlet flows (balance and cooling). For the 0.6 and 0.8%MF cases, the discrepancies are in the same order of magnitude.

Figure 20 shows the measured heating of the cooling mass flowrate from the inlet (MP 10) to the inlet of the lock plate feed cavity (MP 103). As expected with the behavior change in the upstream cavity, this heating is less pronounced for the 1.2%MF case, as there is no mixing between the coolant and the hot gas coming from the main gas path. Figure 20 also detailed the simulation results. The heating is well captured by the simulation for both the 0.6 and 0.8%MF cases while it is over-estimated for the 1.2%MF case. Based on the conclusions of Sec. 4.3, it shows that the hot radial clearances of the upstream labyrinths cavity are suitable for the 0.6% and 0.8%MF cases but probably incorrect for the 1.2%MF case. This influence confirms the importance of the correct specification of the hot build geometry for the accurate prediction of the mass flow distributions and temperatures.

On the first disk rotor, the results show similar trends between the three cases and the conclusions are identical to the reference case (Fig. 21). The simulation under-predicts the measured metal temperatures at the first rotor hub endwall, where unsteady and fully turbulent phenomena occur.

As explained previously, the air temperature at the inlet of the lock plate feed cavity is overestimated by the 1.2%MF whereas it is well predicted for the 0.6 and 0.8%MF cases. However, the discrepancies into the first rotor remain identical for the three cases.

Another calculation with an increased inlet cooling temperature has been carried out and shows that the disk rotor 1 metal temperatures are sensitive to the air temperature at the inlet of the lock plate feed cavity (MP 103).

Thus, as the air temperature at the inlet of the lock plate feed cavity is overestimated for the 1.2% case without any improvement on the rotor disk metal temperatures prediction, it is expected that another phenomenon tends to accentuate the discrepancies with the experimental measures in this specific case. Indeed, as shown by Eastwood [8], even if the cavity is purged, it remains some unsteady

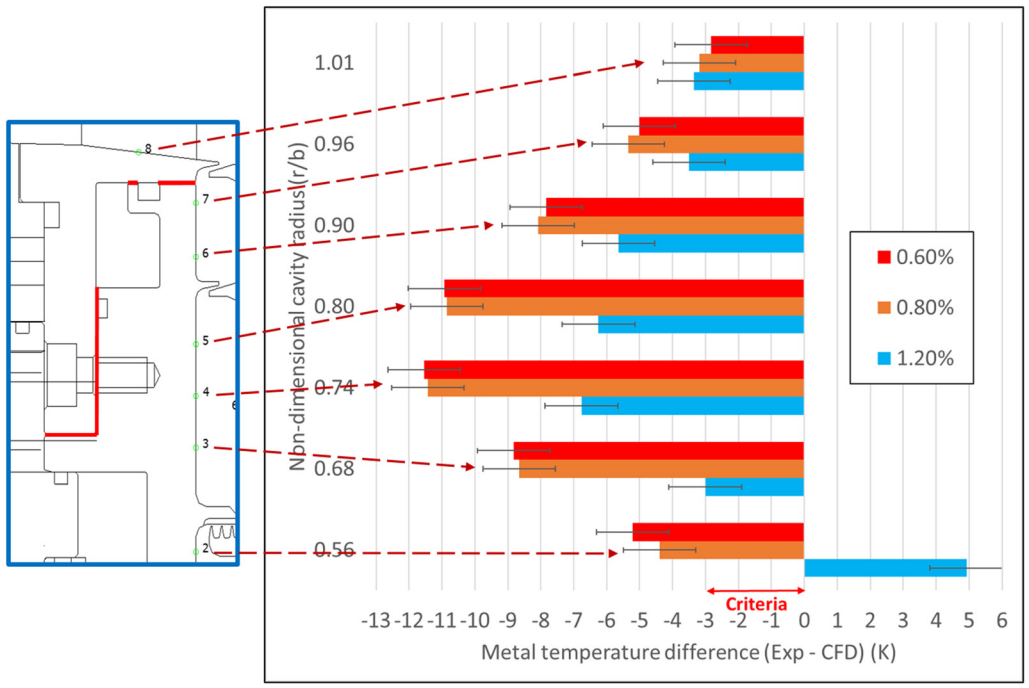

Fig. 19 Difference between the experimental and calculated metal temperatures at the downstream face of the first stator disk for the three cooling flow cases

ingress due to the circumferential pressure variation in the main annulus. As described previously, the RANS simulation is not able to accurately predict theses local phenomena. This could explain why the purged case presents more discrepancies against the experimental data. This result will be confirmed with comparisons against experimental data in the other area of the domain.

In the vicinity of the stator foot, the simulation offers highly accurate results. Comparisons between measured and calculated static pressures on the stator foot show a similar trend between the three cooling configurations: the pressure drop is well predicted by the simulation, with discrepancies below than 30 mbar.

Figures 22 and 23 display the influence of the cooling mass flowrate on the metal and air temperatures prediction on the stator foot. For the three cases, the simulation offers results with a very good accuracy, with discrepancies below the criteria. The conclusions are similar between the 0.6% and 0.8% cases with an overestimation of the measured metal and air temperatures. On the contrary, the simulation underestimates the temperatures for the purged cavity case.

This is probably also due to the unsteady ingresses that occur in the purged case. As the amount of heat coming with theses local ingresses are not captured by the calculation, the metal and air temperatures are too cold by comparison with the experimental data. However, the accuracy of the methodology is not affected by this RANS limitation in that area.

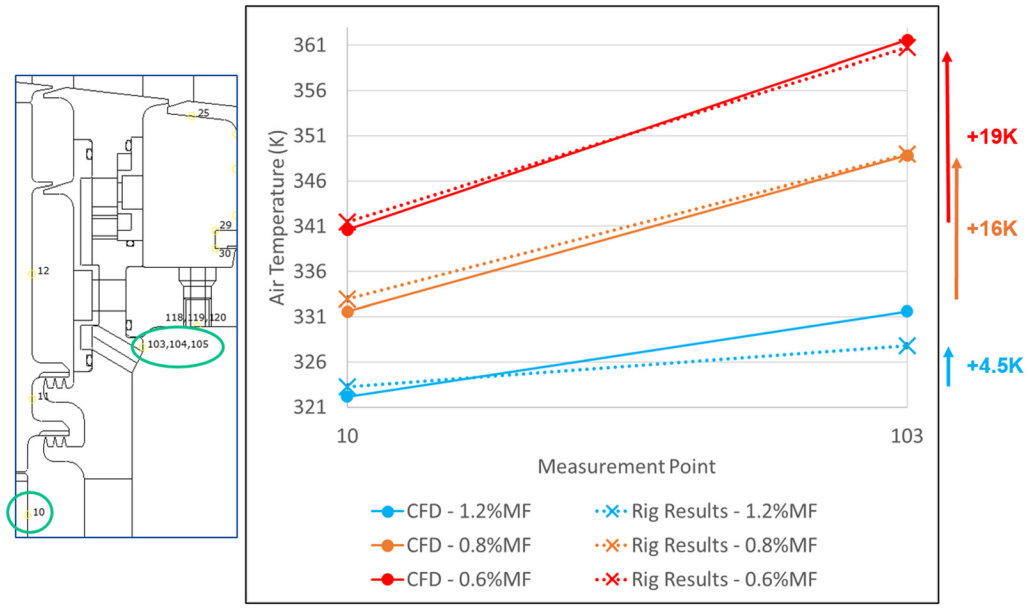

Fig. 20 Warming of the coolant mass flow for the three cases—experimental and numerical results

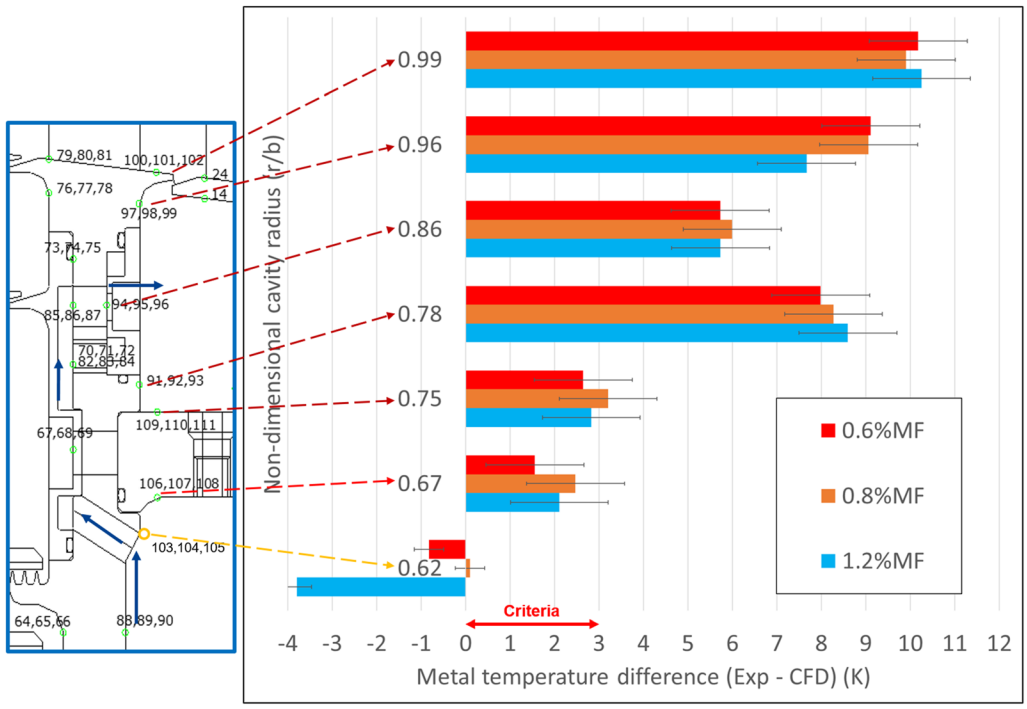

Fig. 21 Difference between the experimental and calculated metal temperatures at the downstream face of the rotor disk 1 for the three cooling flow cases

This behavior can also be observed on the upstream face of the disk rotor 2. Larger differences between predicted and measured metal temperatures are noticed for the purged case. The smallest discrepancies are for the 0.6%MF case. As indicated by the concentration measurements carried out during the MAGPI test campaign [8], the lower the mass flowrate at the rim seal, the stronger the local unsteady egresses or ingresses. The 1.2%MF presents the lowest mass flowrate at the rim seal as indicated in Fig. 18 and so the strongest unsteady ingresses. The more important numerical inaccuracy is then expected and observed for this case (Fig. 24). On the contrary, the 0.6%MF is less sensitive to the numerical limitation, as it has the strongest rim seal mass flowrate. The 0.8%MF case seems to confirm this behavior, with larger predicted/measured metal temperatures differences than the 0.6%MF case, but smaller than the 1.2%MF case. Thus, it is expected but not verified in this study that a strong purged case would give a better accuracy than the 1.2%MF case.

Finally, a good agreement is proposed by the numerical methodology for both the ingress cases with discrepancies lower or close to the criteria, as indicated in Fig. 24. On the contrary, the discrepancies for the 1.2%MF case are higher than the criteria.

To conclude, the influence of the cooling mass flow has shown a good robustness of the methodology, with good accuracy in the stator well area for the three cases.

The discrepancies observed in the reference case on the disks rotor endwall were also seen in the other cooling cases and gave more details about the limitation of the RANS methodology in these areas. It has been observed that the discrepancies are more

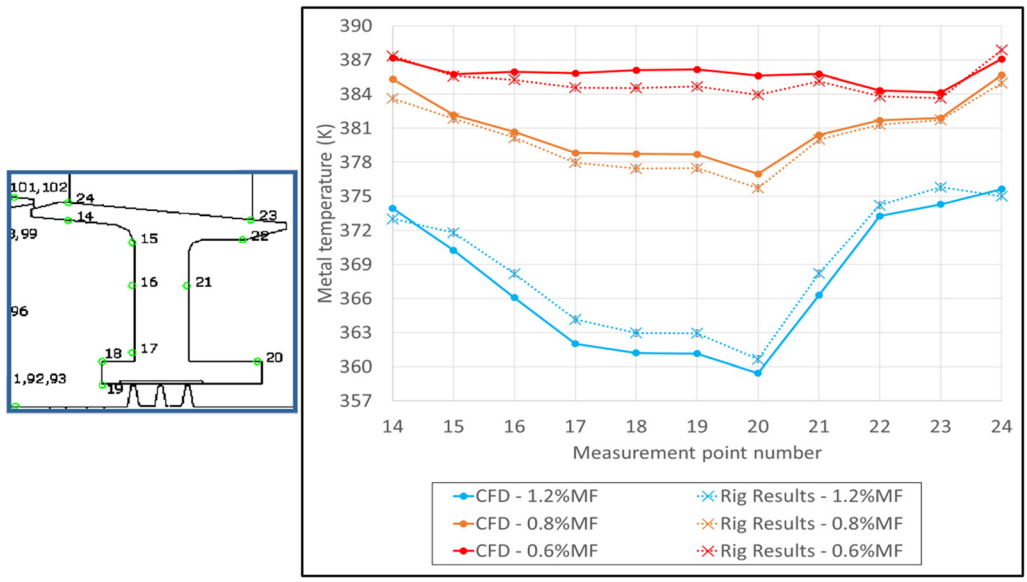

Fig. 22 Stator foot experimental and numerical metal temperatures for the three cooling cases

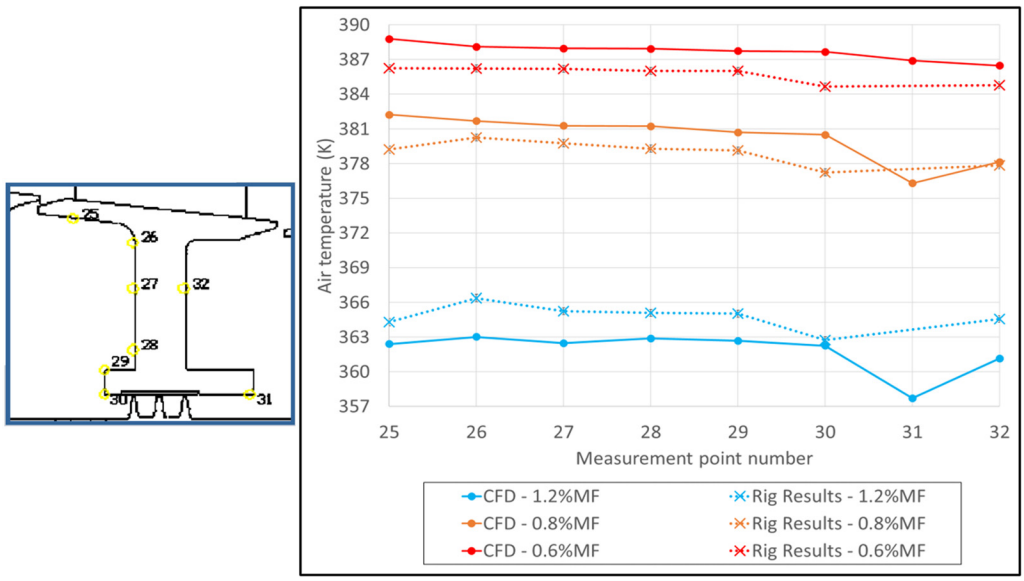

Fig. 23 Stator foot experimental and numerical air temperatures for the three cooling cases

pronounced in cases where the absolute value of the rim seal mass flowrate is weak. The unsteady local ingresses or egresses, observed experimentally and probably poorly captured by the RANS calculations could explain these inaccuracies. Thus, unsteady ingresses in the purged cavity case are not predicted by the calculation and induce the discrepancies shown previously.

Overall, it seems that the more pronounced the cavity behavior (strong ingress with low cooling or strong egress with high cooling flowrate), the more accurate the results.

5 Cooling Flow Rate Influence on the Turbine Performance With Polytropic Efficiency

The numerical methodology presented in this paper may be used to evaluate cooling concepts in terms of thermal effectiveness but also by assessing impact of these technologies on the turbine efficiency. As the calculations use the conjugate heat transfer method with no adiabatic conditions, a special attention must be paid to the efficiency definition.

An efficiency compare an ideal process to a real one. Moreover, as mentioned by Lallemand [10], the ideal process must be associate to the real one. Thus, the well-known isentropic efficiency, which employs an adiabatic and reversible process, must be use with a real adiabatic transformation. The processes consider in this paper are nonadiabatic and must be compared to nonadiabatic ideal processes. The use of the polytropic efficiency allows the comparison of the real process to an associated reversible transformation described with the polytropic work, as follow in Eq. (5) obtained from the study of Pluviose and Perilhon [11]

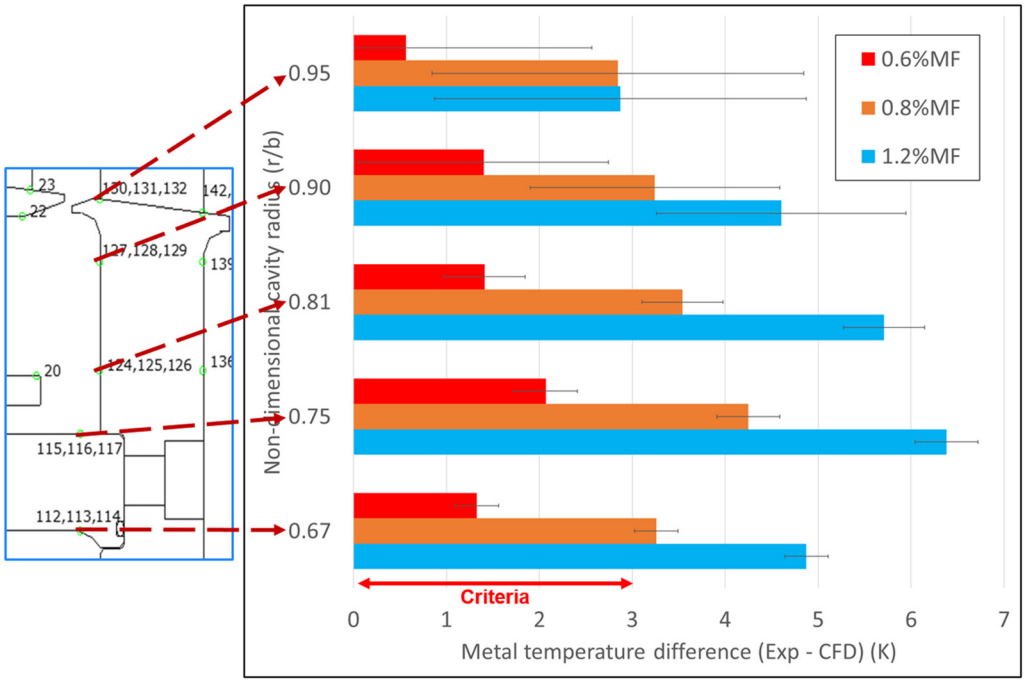

Fig. 24 Difference between the experimental and calculated metal temperatures at the upstream face of the rotor disk 2 for the three cooling flow cases

Table 5 Comparison of the isentropic and polytropic efficiency for different cooling cases

Cases	Main annulus w/o cavities	0.8%MF with cavities	1.2%MF with cavities
Isentropic efficiency η_{is} (%)	93.47	92.53	92.47
Cavities efficiency loss (pts)		−0.94	−1
Polytropic efficiency η_p	92.72	91.59	91.54
Cavities efficiency loss (pts)		−1.133	−1.181
Difference of losses estimation between η_{is} and η_p (pts)	N/A	0.193	0.182

$$W_{\text{polytropic}} = \frac{k}{k-1} r * (T_1 - T_2) + \frac{{V_1}^2 - {V_2}^2}{2} \tag{5}$$

with k, the polytropic coefficient, outlined as follow:

$$k = \frac{1}{\frac{\ln \frac{T_2}{T_1}}{\ln \frac{P_1}{P_2}} + 1} \tag{6}$$

where index 1 and 2 stand for turbine inlet and outlet, respectively.

As the polytropic coefficient is defined with the real inlet and exit temperatures and pressures, the polytropic process is associated with the real one and is then nonadiabatic. This is the main reason of the choice of the polytropic efficiency to evaluate cooling concepts with this methodology.

Finally, the polytropic efficiency is expressed as follow:

$$\eta_p = \frac{\omega * M_{\text{shaft}}}{\dot{m} * W_{\text{polytropic}}} \tag{7}$$

In order to assess the validity of this efficiency, it has been calculated and compared with the isentropic efficiency on the different cooling cases presented previously. Table 5 shows values of the isentropic and polytropic efficiencies for the reference case (0.8%MF) and the purged cavity case (1.2%MF). Table 5 also indicates the efficiency of an ideal adiabatic case containing the main annulus alone and without losses caused by the disk cavities. Thus, the efficiency drop with the cavities is also indicated in the following table, as an efficiency difference with the ideal main annulus case. These losses are of different types, as described by Denton [12].

For the two cases, the conclusions remain the same: whatever the efficiency definition used, a decrease of the turbine efficiency is observed with the inner cavities. Moreover, the trend between the two cooling cases is identical for the two efficiencies, with a lower efficiency for the purged cavity case. However, the polytropic efficiency seems more sensitive to the turbine losses, as it predicts higher efficiency drop than the isentropic efficiency (∼0.2 pts) between the main annulus case and the full domain case.

By calculating the pressure and viscous torques on rotating cavity walls, the windages contribution to the overall efficiency losses was isolated and quantified, as detailed in Eq. (8) and resumed in Table 6. Values are given as absolute efficiency loss and as a percentage of total losses. It shows that the windages are exacerbated with higher cooling flowrate. Thus, as for the overall losses, both efficiencies indicate the same trend for this particular loss

Table 6 Windages efficiency drop with the isentropic and polytropic efficiencies for two cooling flow cases

Cases	0.8%MF	1.2%MF
Windage efficiency loss calculated via η_{is} (pts, %)	−0.290 30.9%	−0.349 34.9%
Windage efficiency loss calculated via η_p (pts, %)	−0.287 25.3%	−0.346 29.3%

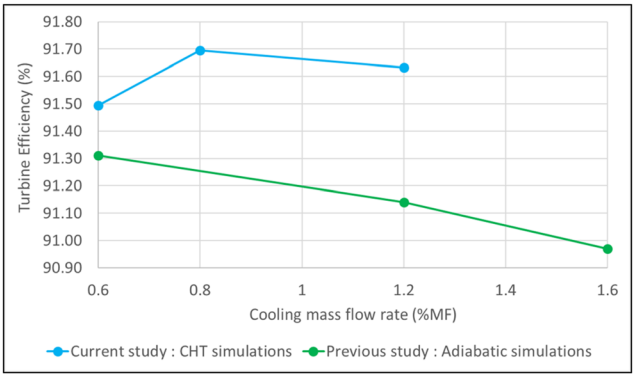

Fig. 25 Influence of the cooling mass flow rate on the turbine efficiency

$$\eta_{\text{windage}} = \frac{\omega * (M_p + M_v)}{\dot{m} * W_{\text{polytropic}}} < 0 \tag{8}$$

with M_p and M_v are the pressure and viscous torques, respectively, calculated on the rotating cavity walls. These values are negative when the fluid takes energy from the shaft, which is the case in this study as the tangential velocity of the fluid is lower than the rotor rotational speed into the major part of the cavities.

With the polytropic efficiency definition, this table shows that the windages account for about a quarter of the total losses for the 0.8% case. The other losses are due to aerodynamic (mixing losses, secondary flow losses…) or thermal (nonadiabatic conditions) causes.

To conclude, a special attention was paid to the efficiency definition. As the calculations carried out use conjugate heat transfer, the polytropic efficiency was chosen in order to consider nonadiabatic conditions into the efficiency definition. Since this efficiency is more sensitive to the turbine losses and follows the same trends as the isentropic efficiency (for overall and windage losses), it confirms that it is a good and accurate tool for assessing the turbine performance.

The polytropic efficiency was then used for the three cooling cases in order to assess the impact of the cooling flowrate on the turbine performance. Figure 25 shows the polytropic efficiency for the three cases, as well as the results coming from previous adiabatic study (isentropic efficiency) [1].

As found by Dixon et al. [1], a decrease of the efficiency is observed between the 0.8%MF case with low ingress and the 1.2%MF case (purged cavity), due to a spoiling effect of the main annulus by the cooling flowrate and accentuated windages. Nevertheless, the difference between these two cases is small and could be within the CFD modeling accuracy. Then, in opposition to the Dixon's study, the lowest efficiency is observed for the 0.6%MF case. Indeed, the thermal losses are higher with lower cooling flowrate and could explain this efficiency drop. As Dixon et al. computed the efficiency values from adiabatic simulations, this effect was not captured and could confirmed the thermal losses influences on the turbine performance.

6 Conclusion

A 3D sectorized RANS CFD model was setup with conjugate heat transfer. In contrast with prior investigations, a different geometry with axial cooling injection through lock plate slots was chosen. Comparisons with the MAGPI experimental data have shown that the methodology gives good results accuracy, in particular in the TSW area. However, discrepancies were observed in the rim regions and have shown the limitations of this type of simulation.

A mesh sensitive study has been done to ensure that the mesh is fine enough. A turbulence model influence has shown that the k–ω SST gives better results than the k–ε model by comparison with the experimental data.

The hot running geometry was used. The estimation of hot radial labyrinths clearances has brought uncertainties which have been assessed. The radial labyrinths clearances have a strong influence on the ingress/egress flows at the rim seal regions, which may have an impact on the results accuracy. In the TSW, air and metal temperatures were not affected by the radial clearance as the ingress flow is weak compared to the cooling flow in that case. This contrasts with the upstream wheelspace where strong influence of the hot geometry was observed on the air and metal temperatures.

Impact of the thermal conditions at the first stator disk has been evaluated, showing significant influence on the upstream wheelspace air and metal temperatures. In order to improve the metal temperature predictions in this area, attention has to be paid on the definition of the thermal boundary conditions and the first stator disk geometry. However, those conditions do not influence the results accuracy on the TSW.

Accuracy of the methodology has been analyzed for three different amounts of cooling mass flow, leading to ingress or egress configurations through the R1/S2 rim seal. For the three cases, good robustness of the methodology was observed, with accuracy results obtained in the stator well area. The limitations of the methodology were highlighted on the disks rotor endwall, especially when the absolute value of the rim seal mass flow is weak. Thus, this methodology seems to proposes the best results for strong ingress or egress case.

Finally, the methodology have shown good results in the prediction of the heat transfer in the stator well area. Therefore, in the future, this type of CFD model may be used to evaluate cooling concepts in terms of thermal effectiveness but also by assessing impact of these technologies on the turbine efficiency.

Acknowledgment

The authors would like to acknowledge Safran Aircraft Engines specialists and ANSYS for their technical support, advice using the FLUENT software and for the technical validation of this work. A special mention must be made to the MAGPI team for all the data that was provided, making this study achievable. The present investigation is supported by ANRT (Association Nationale de la Recherche et de la Technologie).

Data Availability Statement

The datasets generated and supporting the findings of this article are obtainable from the corresponding author upon reasonable request.

Nomenclature

Symbols

A = cross-sectional area (m^2)
b = upstream wheelspace rim seal radius (m)
C_D = discharge coefficient
$\dot{m}$ = mass flow rate (kg s^{-1})
M_p = pressure torque (N·m)
M_v = viscous torque (N·m)
M_{shaft} = torque on the turbine shaft (N·m)
P = static pressure (Pa)
P_0 = total pressure (Pa)
R = gas constant (J kg^{-1} K^{-1})
T = static temperature (K)
T_m = metal temperature (K)
T_0 = total temperature (K)
$W_{polytropic}$ = polytropic work (J kg^{-1})
γ = Laplace coefficient
λ = thermal conductivity (W m^{-1} K^{-1})
μ = dynamic viscosity (kg m^{-1} s^{-1})
ω = rotational speed (rad s^{-1})

Abbreviations

CFD = computational fluid dynamics
FEA = finite element analysis
MAGPI = main annulus gas path interaction
MP = measurement point
NGV = nozzle guide vane
RANS = Reynolds-averaged Navier–Stokes
RPM = rounds per minute
R1/S2 = rotor 1/stator 2
TSW = turbine stator well

References

[1] Dixon, J. A., Valencia, A. G., Coren, D., Eastwood, D., and Long, C., 2014, "Main Annulus Gas Path Interactions—Turbine Stator Well Heat Transfer," ASME J. Turbomach., **136**(2), p. 021010.
[2] Pohl, J., 2016, "Turbine Stator Well Heat Transfer and Design Optimisation Using Numerical Methods," Ph.D. thesis, University of Leeds, Leeds, UK.
[3] Smith, P. E. J., Mugglestone, J., Tham, K. M., Long, C. A., and Coren, D. D., 2012, "Conjugate Heat Transfer CFD Analysis in Turbine Disc Cavities," ASME Paper No. GT2012-69597.
[4] Da Soghe, R., 2011, "Numerical Investigation of Flow and Heat Transfer in Stator Well Cavities of a Two-Stages Axial Turbine," Ph.D. thesis, Università degli Studi di Firenze, Florence, Italy.
[5] Lück, H., Schäfer, M., and Schiffer, H., 2014, "Simulation of Thermal Fluid-Structure Interaction in Blade-Disc Configuration of an Aircraft Turbine Model," ASME Paper No. GT2014-26316.
[6] Dixon, J. A., Valencia, A. G., Bauknecht, A., Coren, D., and Atkins, N., 2013, "Heat Transfer in Turbine Hub Cavities Adjacent to the Main Gas Path," ASME J. Turbomach., **135**(2), p. 021025.
[7] Coren, D. D., Atkins, N. R., Turner, J. R., Eastwood, D. E., Davies, S., Child, P. R. N., Dixon, J. A., and Scanlon, T. J., 2013, "An Advanced Multiconfiguration Stator Well Cooling Test Facility," ASME J. Turbomach., **135**(1), p. 011003.
[8] Eastwood, D., 2014, "Investigation of Rim Seal Exchange and Coolant Re-Ingestion in Rotor Stator Cavities Using Concentration Techniques," Ph.D. thesis, University of Sussex, Brighton, UK.
[9] ANSYS FLUENT, 2022, "ANSYS FLUENT Theory Guide," ANSYS FLUENT, Canonsburg, PA.
[10] Lallemand, A., 2003, "Compression et Détente Des Gaz ou Des Vapeurs," Techniques de L'Ingénieur, INSA, Lyon, France.
[11] Pluviose, M., and Perilhon, C., 2003, "Turbomachines-Thermodynamique de la Conversion d'énergie," Techniques de L'Ingénieur, CNAM, Paris, France.
[12] Denton, J. D., 1993, "Loss Mechanisms in Turbomachines," ASME Paper No. 93-GT-435.